

Numerical and Experimental Investigation of Blended Wing Body Configuration

Midhun MV¹, Partha Mondal², Pawan Kumar Karn³ & Priyank Kumar⁴

Department of Space Engineering and Rocketry,
Birla Institute of Technology, Mesra, Ranchi-835215

ABSTRACT

Blended Wing Body (BWB) configuration is an unconventional aircraft design in which the wing and fuselage are blended to form an aircraft. Researches have shown that this design concept offers a significant improvement in the aerodynamic efficiency, yet the concept has to be developed for the commercial transport aircrafts. A 3-D BWB model is designed, and then numerical and experimental analyses are carried out. Aerodynamic characteristics and flow features obtained from the OpenFOAM data have been studied, analysed and compared with the wind tunnel results. The model designed has shown satisfied results and can operate at high angles of attack.

Key Words: Blended Wing Body, Aerodynamics, OpenFOAM, Flow Visualization, Wind Tunnel

1. Introduction

Ever since the first aircraft designed and flown by Wright Brothers in 1903, many improvements were done to achieve better design and performances. But much of the advancements were made in the aerodynamics, propulsion systems, structures, materials and electronics and apart from the minor changes, the blueprint of the airplane geometry i.e. the classic tube and wing design has always been constant. With the increasing concern for the environment and the depleting fuels, research has been going on to develop a more efficient and environmentally friendly aircrafts, hence unconventional designs are gaining popularity in the recent decades. The unconventional aircraft designs such as Flying Wing and Blended Wing Body configurations etc. have shown potential which otherwise might be impossible to achieve.

Blended Wing Body configuration has an unconventional design in which the wing and fuselage are blended to form an aircraft. Researches have shown that this design concept offers a significant improvement in the aerodynamic efficiency compared to the conventional aircraft yet the concept has to be developed for the commercial transport aircrafts [1]. The BWB concept has been inspired from the flying wing aircraft, it combined the aerodynamic advantages of flying wing with the loading capabilities of that of traditional aircraft, by increasing the volume of the wing at the center to act as a fuselage. This allows BWB aircraft to carry more passengers and cargos. Some conceptual Unmanned Air Vehicle (UAV) designed based on the blended delta wing-body configurations exhibit vortex-dominated flows. Research has reported some aerodynamic, stability and control issues for these configurations [1].

In the late 90s, Liebeck et al. [2] introduced the Blended Wing Body configuration as a subsonic commercial transport which offered great advantages in terms of performance over the conventional, transonic transports. Roberto Merino-Martinez [3] designed a BWB aircraft baseline and studied its aerodynamic performance and the Euler-based shape optimization were done considering its challenging stability and control features. Qin et al. [5] presented the aerodynamic study of blended wing body configuration designed under the European project, MOB. Richard J. Re [6] performed an experimental investigation to obtain force balance and wing pressure data on a 0.017 scaled model of an early blended-wing-body double deck subsonic transport configuration (without propulsion systems installation) with and without winglet. Ammar et al. [7] designed a 200 passengers capacity BWB aircraft and compared its aerodynamic performance with A320 aircraft with an emphasis on the stability of the aircraft. Dehpanah et al. [10] studied the aerodynamic aspects of different blended wing body airframe using computational analysis. Thompson et al. [11] constructed a 5m wingspan BWB UAV equipped with full navigation and autopilot system.

1 Master's student 2 Assistant Professor: pmondal@gmail.com
3 PhD student 4 Assistant Professor

The present work focuses on the aerodynamic study of the blended wing body configuration at low subsonic speed. A 3-D BWB model is designed in SolidWorks and fabricated using 3D printer. The computational analysis is carried out using the open source software, OpenFOAM [8], and the wind tunnel experiments are performed at an air speed of 20m/s. In both the analyses, Lift Coefficient (C_L) and Drag Coefficient (C_D) are computed with respect to the variation of angle of attack. Pressure distribution, pathlines and limiting streamlines on the surface of the BWB model are also extracted from the CFD data to study the flow over the 3D model. Tuft flow visualization is done to observe the flow pattern around the BWB at various angles of attack.

2. Methodology

Step 1: Designing and Fabrication of the BWB Model

The current BWB model design is inspired from some of the measurements from the Roberto Merino Martinez's thesis [3] and the aerofoil selections are based on the paper of Carlsson et al. [4]. The geometry is composed of centre body, inner wing and an outer wing which were then "blended" to form the BWB. The propulsion systems are not included in the current BWB design, although its importance is fully appreciated. The BWB model consists of 2 aerofoil profiles, NACA 0017 and NACA 0012, which are placed at 6 different sections, defining the geometry.

- NACA 0017, centre of the model, from 0mm to 0.35mm.
- NACA 0017, from 0.35mm to 41.5mm, comprising the fuselage
- NACA 0012, from 41.5mm to 52.28mm, inner wing
- NACA 0012, from 52.28mm to 62.35mm, inner wing
- NACA 0012, from 62.35mm to 82.21mm, comprising the outer wing
- NACA 0012, at the tip of the wing

The airfoil coordinates were generated using the airfoil generator of Airfoil Tools [9]. Figure 1 shows the BWB model. Table 1 shows the specifications of the current BWB model. All the aerodynamic coefficients presented in this paper are based on this reference area mentioned in Table 1.

The model used for experiments is fabricated using a 3D Printer. The designed CAD model is imported into software for 3D printing. Fused filament fabrication (FFF) process is used for the fabrication and the material used is Acrylonitrile Butadiene Styrene (ABS) plastic. The BWB model is printed in two halves and then combined to form the whole geometry. The model is then coated with some layers of spray paint to increase the smoothness of the surface. The half model is used for the computational analysis whereas the experiments are carried out using the full model.

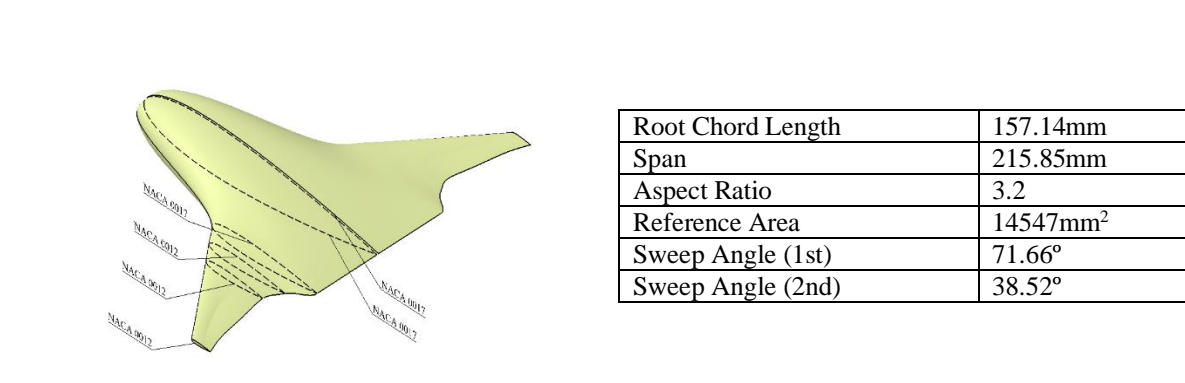


Figure 1: Blended Wing Body (BWB) model

Table 1: Specifications of the current BWB model

Step 2: Structured Grid Generation

Mesh is generated around the half model using the commercial meshing software, GAMBIT. Two C-type grid domains are generated around model to produce a structured grid in the computational domain. The far-field is 20 times the root chord of the blended wing body. Grid stretching is used to concentrate the mesh

accordingly over the model and domain. The grid used for the simulation is hexahedral structured grid everywhere except the tip of the wing where hex/wedge type with cooper scheme grid is generated. The adjacent plane to the model act as symmetry plane. The boundary conditions specified for the grid are shown in Figure 2. The y^+ value of the first grid point off the wall was taken as 50. The mesh contains 2.1 million cells and was generated considering the use of a wall function. Figure 3 shows a closer view of the mesh on the model.

Step 3: Simulation Using OpenFOAM

The mesh is then converted to OpenFOAM [8] format for the analysis. The simulation is carried out for a steady-state, incompressible flow with a velocity of 20m/s corresponding to Reynolds Number of 2.1×10^5 based on the root chord. simpleFoam solver with Spalart-Allmaras turbulence model is used for the simulation. Aerodynamics characteristics such as C_L , C_D at various angles of attack are computed and pressure contours, pathlines are obtained from the solutions at various angles of attack.

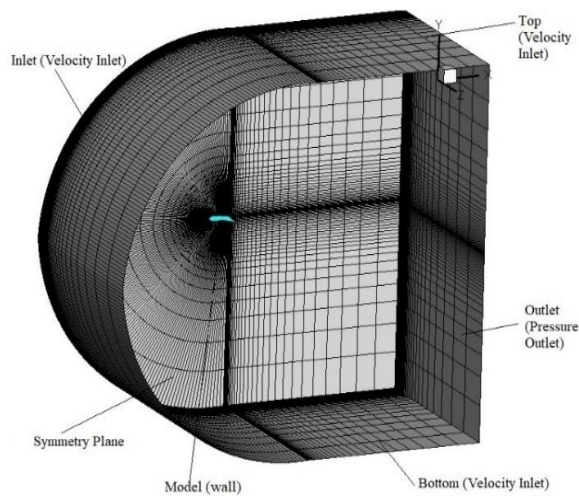


Figure 2: Boundary conditions used for the domain

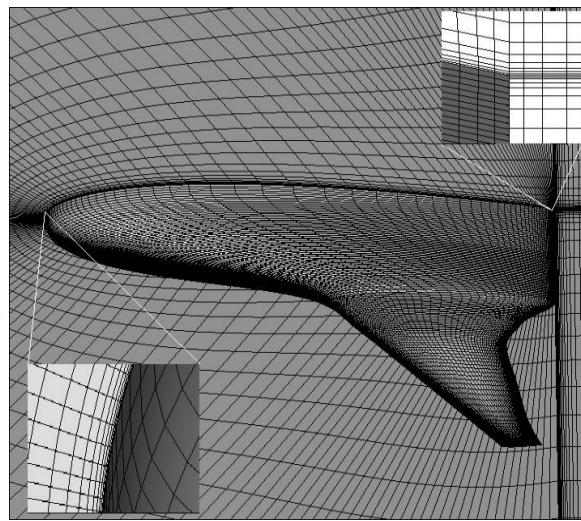


Figure 3: Closer view of the mesh over the model

Step 4: Experimental Analysis

All experiments are conducted using the low subsonic wind tunnel available at the Aerodynamic Lab., Department of Space Engineering and Rocketry, BIT Mesra, Ranchi. This wind tunnel has a test section of 600mm x 600mm x 1200mm. It is a suction type, open circuit continuous flow fan driven wind tunnel. Quantitative and Qualitative analyses are performed at different angles of attack to study the flow physics of the BWB model. Quantitative analysis includes the measurement of forces using strain gauge balance. Qualitative analysis is made using the tuft flow visualisation technique. Figure 4 shows the BWB model placed in the wind tunnel for the force measurements. Experiments are carried out on the 3-D Blended Wing Body model fabricated using 3-D printer (Figure 5). The experiments are performed at a velocity of 20m/s and Reynolds number of 2.1×10^5 based on the root chord from $\alpha=0^\circ$ to $\alpha=50^\circ$ with an increment of 5° step.



Figure 4: BWB model placed in the wind tunnel



Figure 5: 3-D Printer with the fabricated model

3. Results and Discussions

This section presents the results obtained from the CFD and the experimental analyses of the blended wing body configuration. The results obtained are analysed and discussed to understand the flow behaviour over the BWB model. The CFD results are then compared with the experimental data.

3.1 Aerodynamic Characteristics of BWB

3.1.1 Force Coefficients

Aerodynamic force coefficients which include the lift and the drag coefficients acting over the model are computed for the different angles of attack.

Figure 6 shows the variation of the lift coefficient (C_L) for different angles of attack (α) varying from 0° to 60° . The lift curve increases with the increase in angle of attack up to 40° . Increasing the angle of attack beyond 45° , the flow will fully separate from the body. At this point, the C_L starts decreasing with the angle of attack, and the body said to be stalled. This suggests that the BWB model is stalled at $\alpha = 45^\circ$.

Figure 7 shows the variation of the drag coefficient (C_D) for different angles of attack (α) varying from 0° to 60° . At low angle of attack ($\alpha < 10^\circ$), the value of C_D is small and its variation is not significant with increasing the angle of attack. As the angle of attack is increased beyond $\alpha = 10^\circ$, C_D continues to increase.

The computational results match closely with the experimental data. However, at higher angle of attack, computational values start deviating from the experimental data, particularly in the prediction of drag.

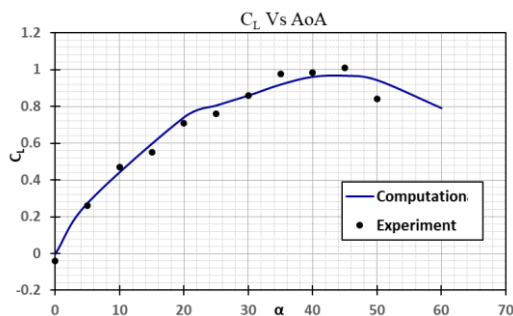


Figure 6: Variation of C_L with angle of attack

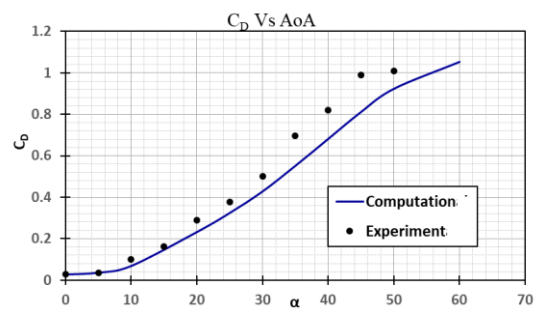


Figure 7: Variation of C_D with angle of attack

3.1.2 Lift/Drag Ratio and Drag Polar

Figure 8 shows the variation of the Lift to Drag ratio (L/D) for different angles of attack (α) varying from 0° to 60° obtained from the computational and experimental analyses. The maximum value of L/D is achieved at an angle of attack 6° . Hence, the optimum flight configuration of the present BWB body will be at $\alpha = 6^\circ$.

Figure 9 shows the drag polar for the BWB model. Initially, the change of C_L is sharp then it increases gradually. On the other hand, C_D increases sharply at large angle of attack. This is due to the fact that at large angle of attack, the separated region is increased. This will finally increase the pressure drag and affect the generation of lift. Therefore, the total drag acting on the model is also increased.

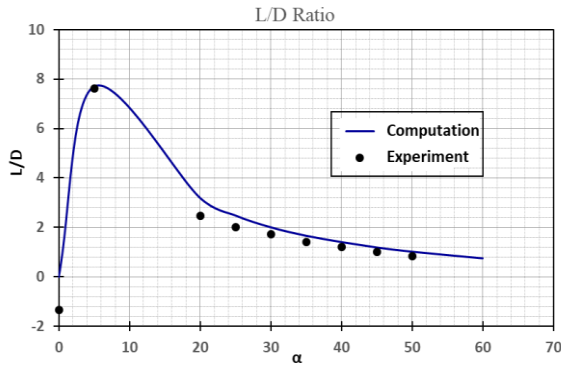


Figure 8: Variation of L/D with angle of attack

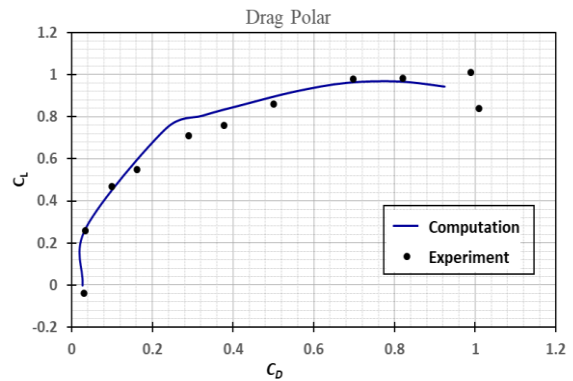


Figure 9: Drag Polar for the BWB

3.2 Pressure Coefficient Distribution

C_p distributions are plotted at specified spanwise locations ($y/(b/2)$): 0.1, 0.5, 0.7, and 0.9 for the BWB model for various angles of attack. Pressure coefficient distributions at spanwise locations for different angles of attack are shown in Figure 10.

3.2.1 Section at $y/(b/2) = 0.1$

C_p is measured at the 10% of the half span of the body. The aerofoil at this section is NACA 0017. For 0° angle of attack, since the aerofoil used is symmetrical aerofoil, C_p values for the upper and lower surface overlap over each other at all the locations. Figure 10(a) shows the C_p distribution at 0° .

At $\alpha = 20^\circ$, there is a suction peak near the leading edge, then the pressure increases gradually as we move downstream of the body as seen in Figure 10(b).

At $\alpha = 30^\circ$, the pressure near the leading edge is lower than the ambient pressure and then gradually increases as we move downstream till around 50% of the chord. After that, C_p starts decreasing for some time and at the trailing edge it is almost equals the ambient pressure. Figure 10(c) shows the C_p distribution at 30° .

At $\alpha = 40^\circ$, the pressure gradually increases till around 40% of the chord. After this, C_p starts decreasing and then becomes constant after $x/c = 0.5$ as shown in Figure 10(d).

At $\alpha = 50^\circ$, the region will have vortical air which forms stirred up wake region. Figure 10(e) shows the C_p distribution at AoA of 50° .

At $\alpha = 60^\circ$, the large separated and vortical flow is observed all over the body. Due to this flow feature, less lift is produced. C_p distribution at AoA of 60° is shown in Figure 10(f).

3.2.2 Section at $y/(b/2) = 0.5$

C_p is measured at the 50% of the half span of the body. The aerofoil at this section is NACA 0017. At $\alpha = 20^\circ$, the C_p value is constant all over the body. The flow has separated at this section. Figure 10(b) shows the

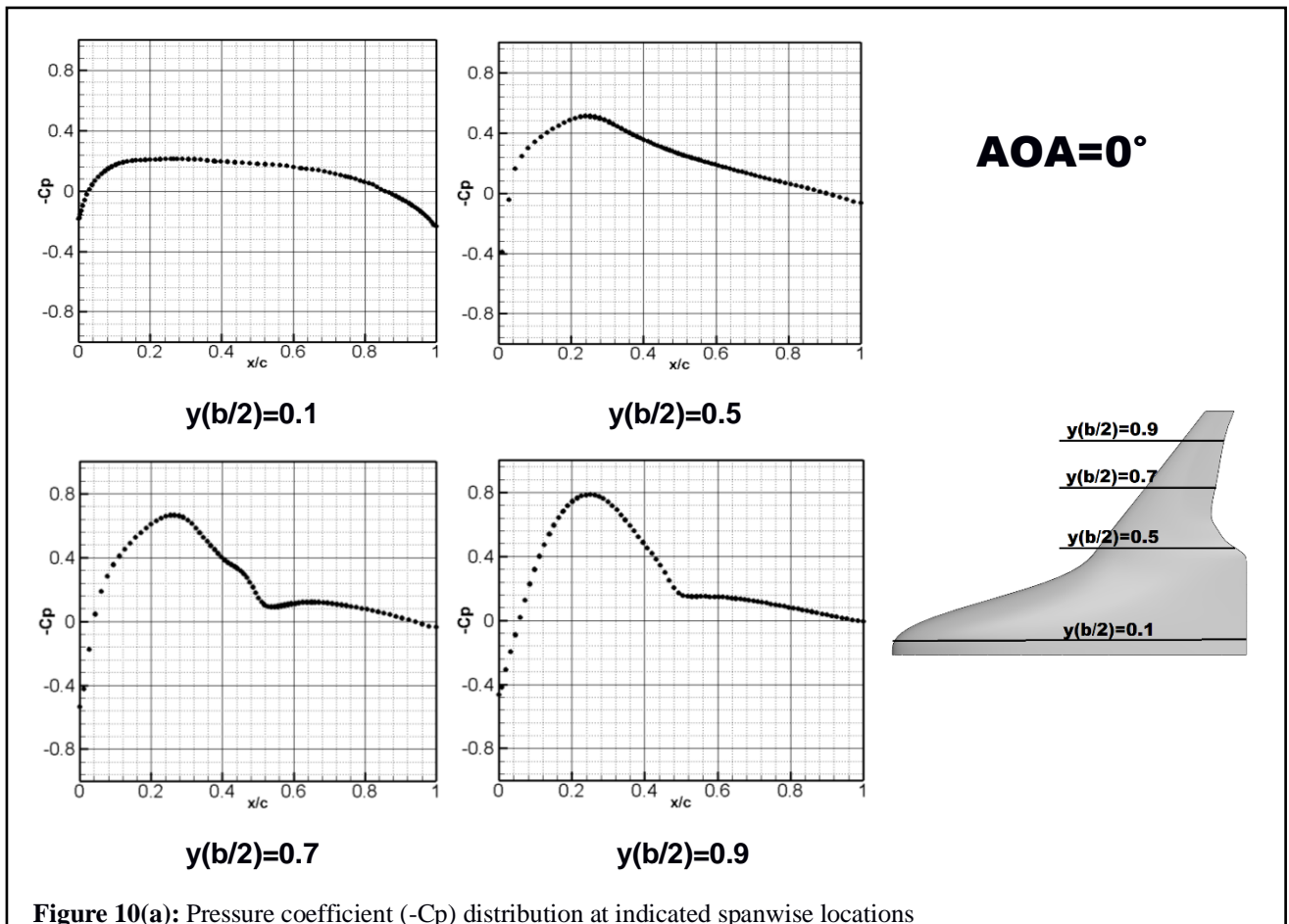
Cp distribution at 20°. After separation, the Cp value all over the separated region becomes constant and the pressure is lower than the ambient pressure. Beyond angle of attack 20°, the Cp distribution shows a similar trend. The flow is fully separated on the upper surface at this section but the body will produce lift because the flow over the centre body will produce lift till the angle of attack 40°.

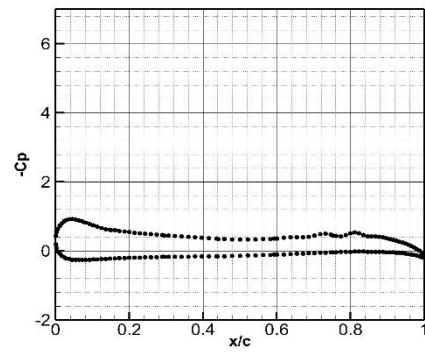
3.2.3 Section at $y/(b/2) = 0.7$

Cp is measured at the 70% of the half span of the body. The aerofoil at this section is NACA 0012. As mentioned earlier, beyond 20° angle of attack, the flow is fully separated at this wing region and the wing is stalled. At angle of attack 20°, the Cp value is very low at the leading edge and then a sudden increase is observed and after that it becomes flat. Beyond angle of attack 20°, the Cp distribution shows a similar trend.

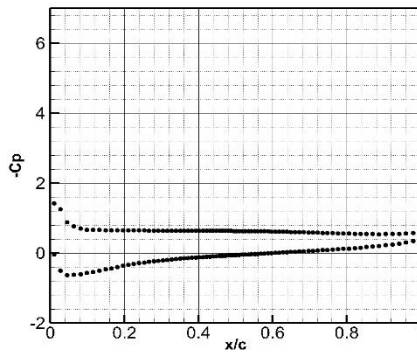
3.2.4 Section at $y/(b/2) = 0.9$

Cp is measured at the 90% of the half span of the body. The aerofoil at this section is NACA 0012. At $\alpha = 20^\circ$, near the leading edge, Cp increases till 25% of the chord and then becomes flat. Similar trend is observed for other angle of attack also.

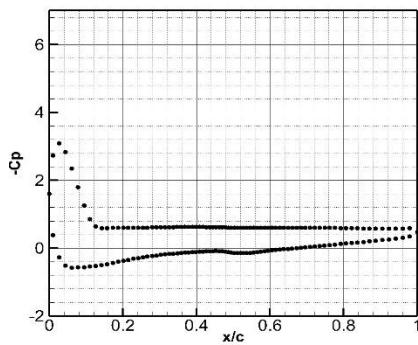




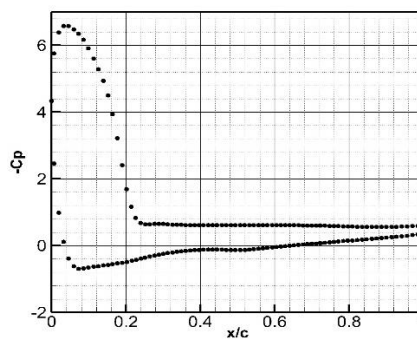
$y(b/2)=0.1$



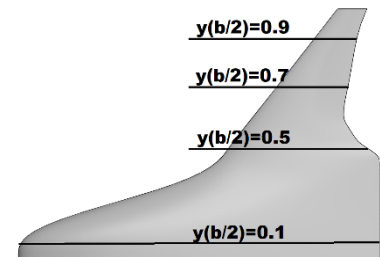
$y(b/2)=0.5$



$y(b/2)=0.7$

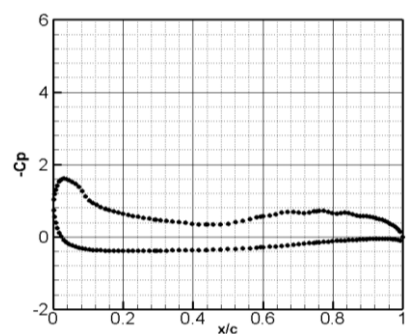


$y(b/2)=0.9$

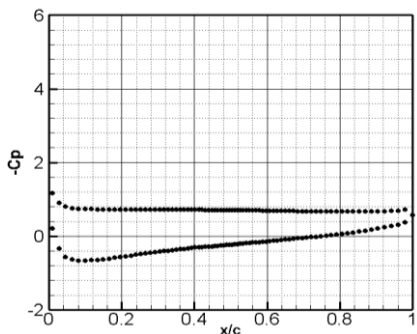


$AOA=20^\circ$

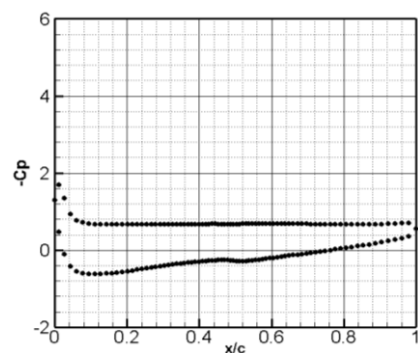
Figure 10(b): Pressure coefficient ($-C_p$) distribution at indicated spanwise locations



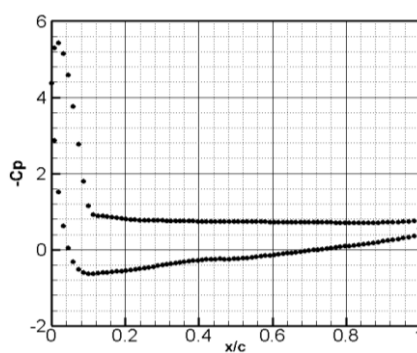
$y(b/2)=0.1$



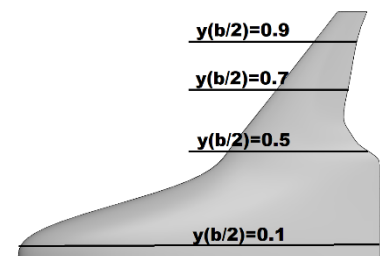
$y(b/2)=0.5$



$y(b/2)=0.7$

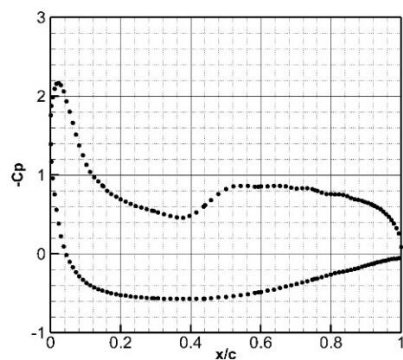


$y(b/2)=0.9$

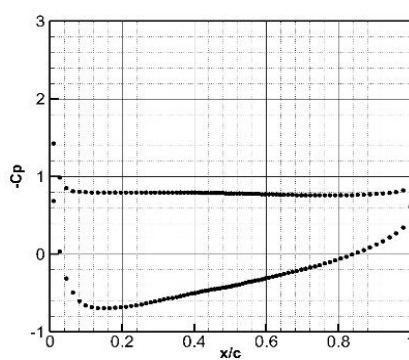


$AOA=30^\circ$

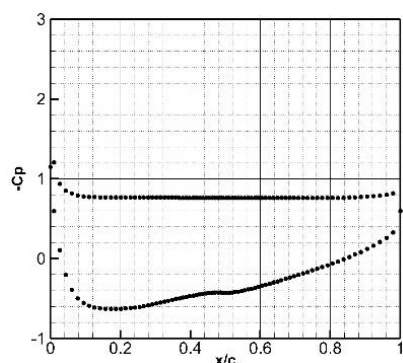
Figure 10(c): Pressure coefficient ($-C_p$) distribution at indicated spanwise locations



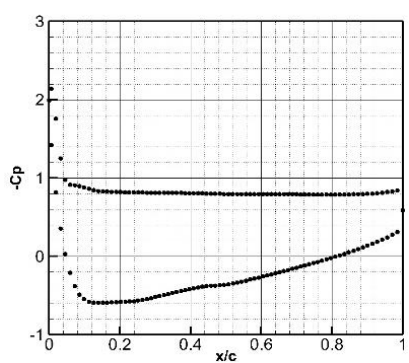
$y(b/2)=0.1$



$y(b/2)=0.5$



$y(b/2)=0.7$



$y(b/2)=0.9$

$AOA=40^\circ$

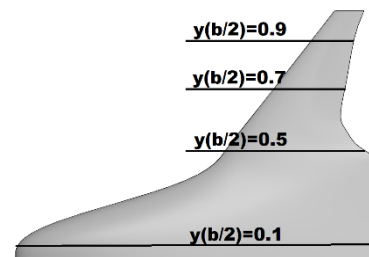
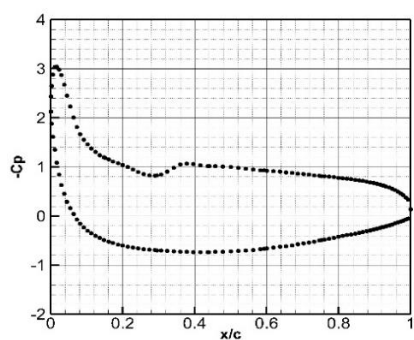
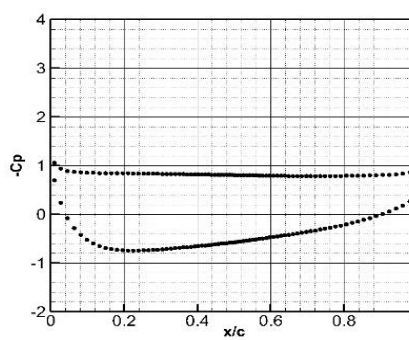


Figure 10(d): Pressure coefficient ($-C_p$) distribution at indicated spanwise locations

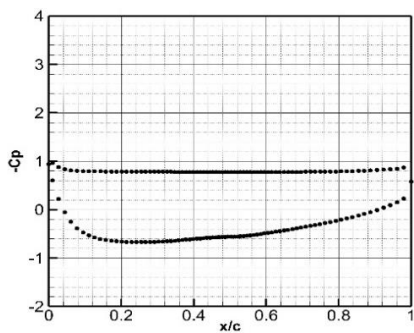


$y(b/2)=0.1$

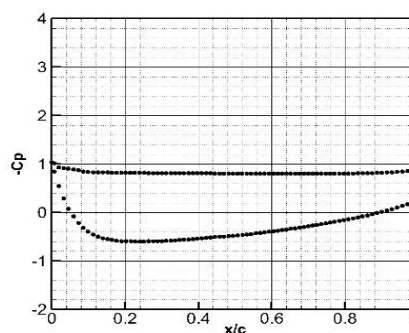


$y(b/2)=0.5$

$AOA=50^\circ$



$y(b/2)=0.7$



$y(b/2)=0.9$

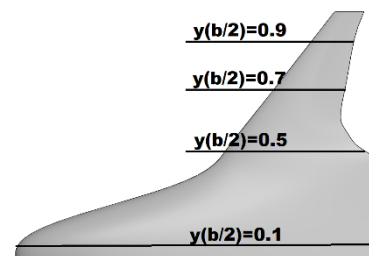
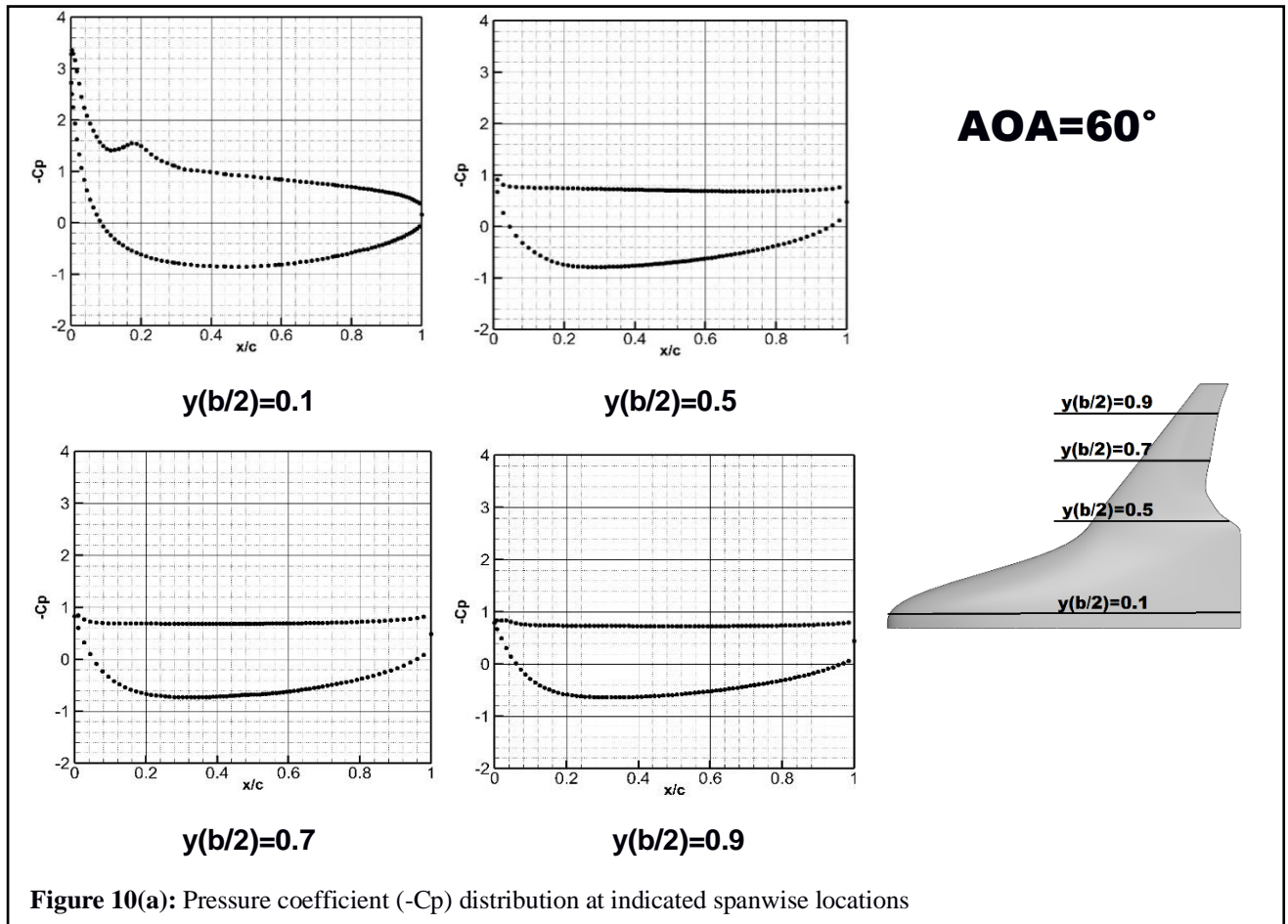


Figure 10(e): Pressure coefficient ($-C_p$) distribution at indicated spanwise locations



3.3 Flow Visualizations

3.3.1 Pathlines at different angle of attack

The flow over the BWB model changes with the increase in the angle of attack. To visualise the flow behaviour over the BWB model, pathlines of the flow are created. Figure 11 shows the pathlines over the model at different angles of attack.

At $\alpha = 0^\circ$, the flow over the model leaves smoothly. The flow is attached to the surface of the model and no lift is produced as the aerofoils are symmetrical. At $\alpha = 20^\circ$, the flow has separated at the wing. But the body continues to produce lift due to the fuselage part even when the wing is stalled.

At $\alpha = 30^\circ$, the more vortices start building up over the body. Beyond $\alpha = 40^\circ$, the flow will separate all over the body. The vortex starts lifting off the body in the circulation zone. The flow will be vortical over the surface of the body and the whole body is stalled.

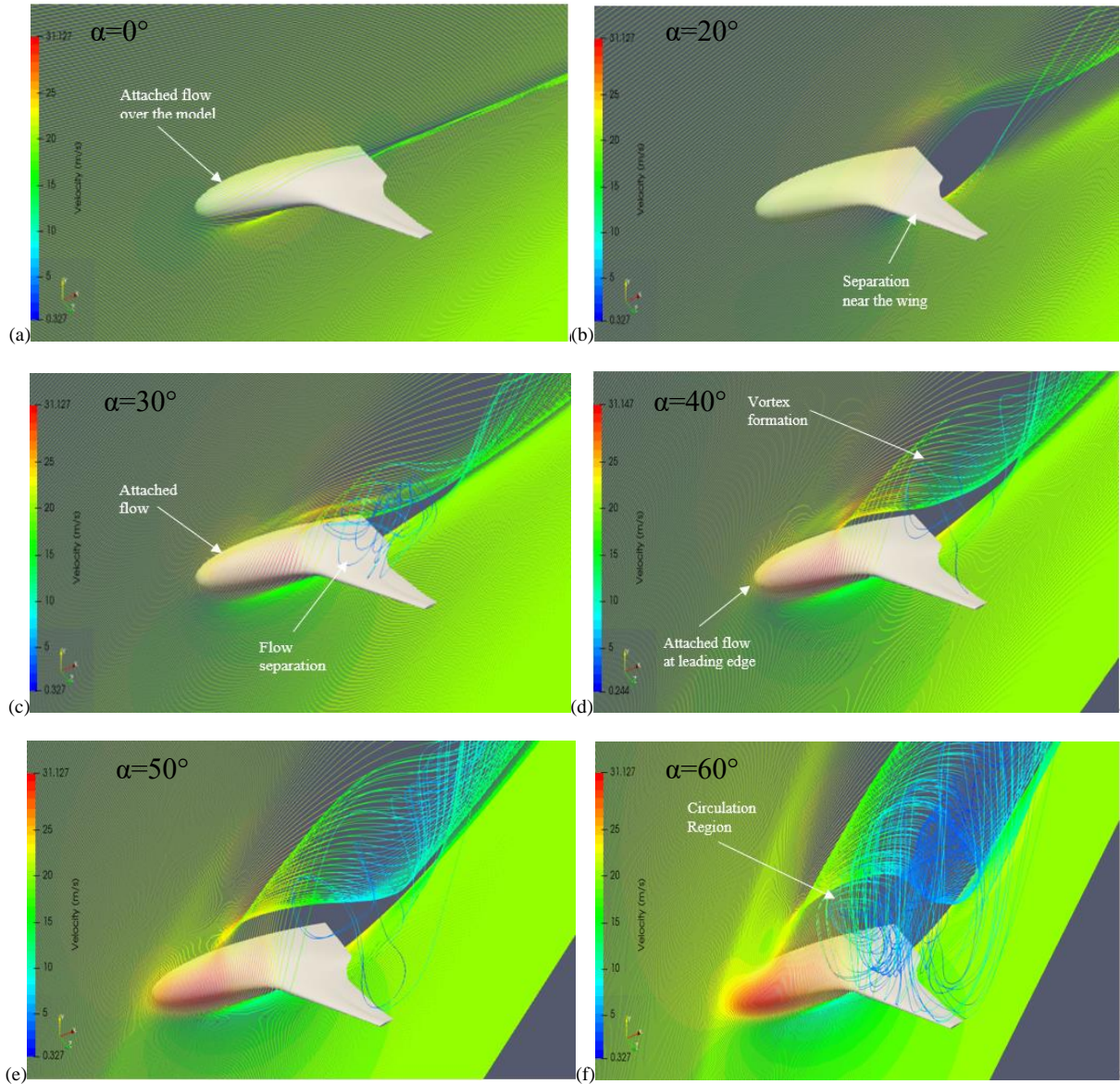


Figure 11: Pathlines over the BWB model at different angles of attack

3.3.2 Streamlines over the top surface at different Angle of Attack

Streamlines were visualised on the upper surface of the BWB model to get a better understanding of the flow over the model at different angles of attack. Figure 12 shows the surface limiting streamlines over the BWB model at different angles of attack.

At angle of attack 0° , the streamlines are straight and attached to the body. With the increase in the angle of attack, flow starts to separate. At angle of attack 20° , the streamlines near the leading-edge show that separation has occurred. Small circulation region is also observed over the wing.

At angle of attack 30° , the separated region is increased. Increasing the angle of attack, the vortices are spreading up over the body. This can be observed from the streamlines as shown in Figures 12(d)-(e).

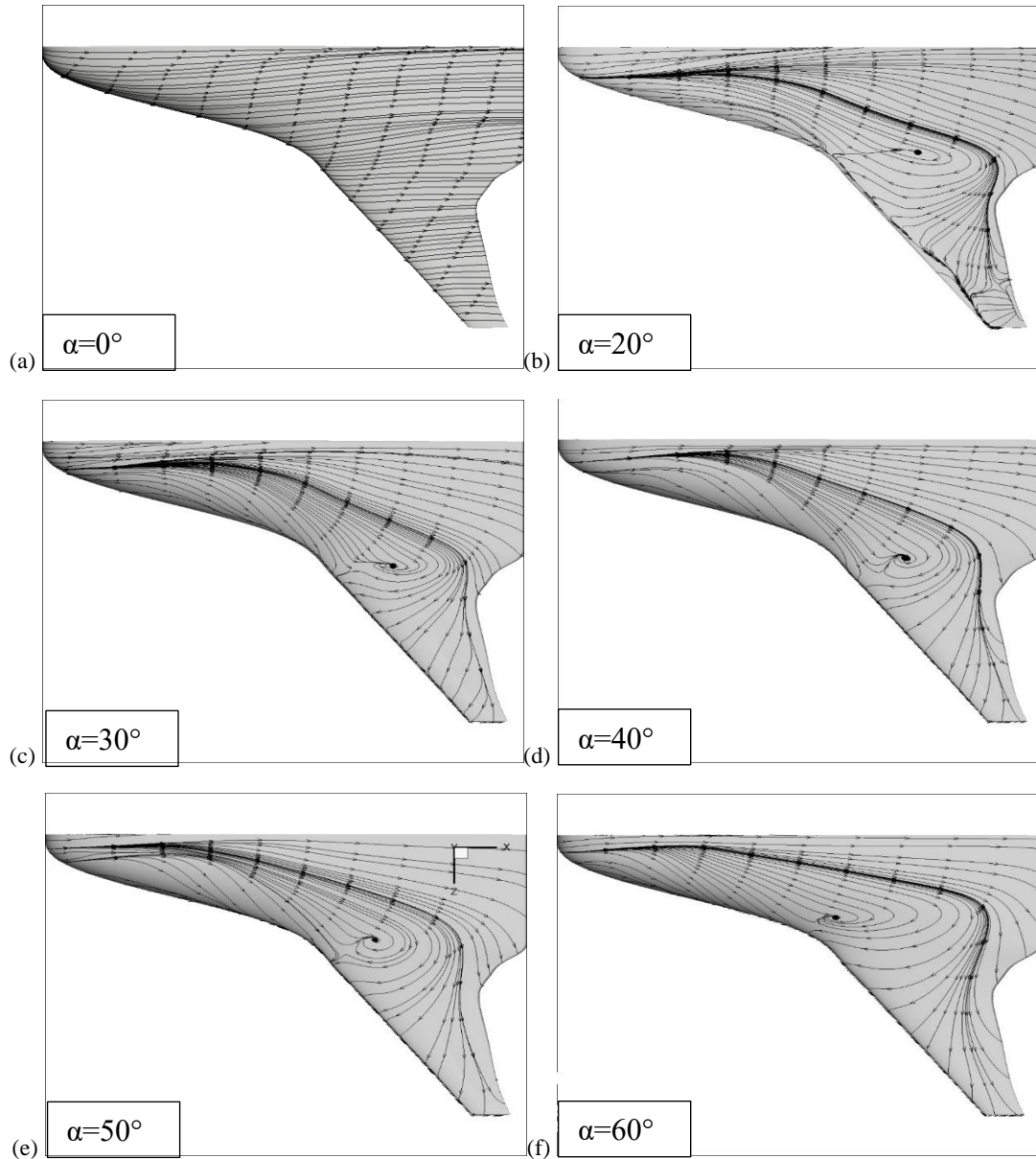


Figure 12: Surface streamline over the BWB model at different angles of attack

3.3.3 Tuft Flow Visualization

Visualization using tuft during wind tunnel tests is also done to complete the analysis. Tufts will align itself accordingly as air flows over the model. The tuft flow visualisation was carried out for angle of attack from 0° to 50° . Figure 13 shows the tuft flow at major angles of attack.

At angle of attack 0° , the tufts are arranged in the direction of the flow all over the model. The flow is attached to the surface. At angle of attack 15° , the flow is separated at the wings. This is indicated by the reverse tufts' direction on the wing (Figure 13(b)).

At $\alpha = 30^\circ$, the tufts are oscillating over the wing region indicating the occurrences of vortical flow but at the leading edge of the center body, the tufts are aligned with the flow direction. At $\alpha = 50^\circ$, the tufts all over the model are oscillating, hence the flow is fully vortical over the model (Figure 12(d)).

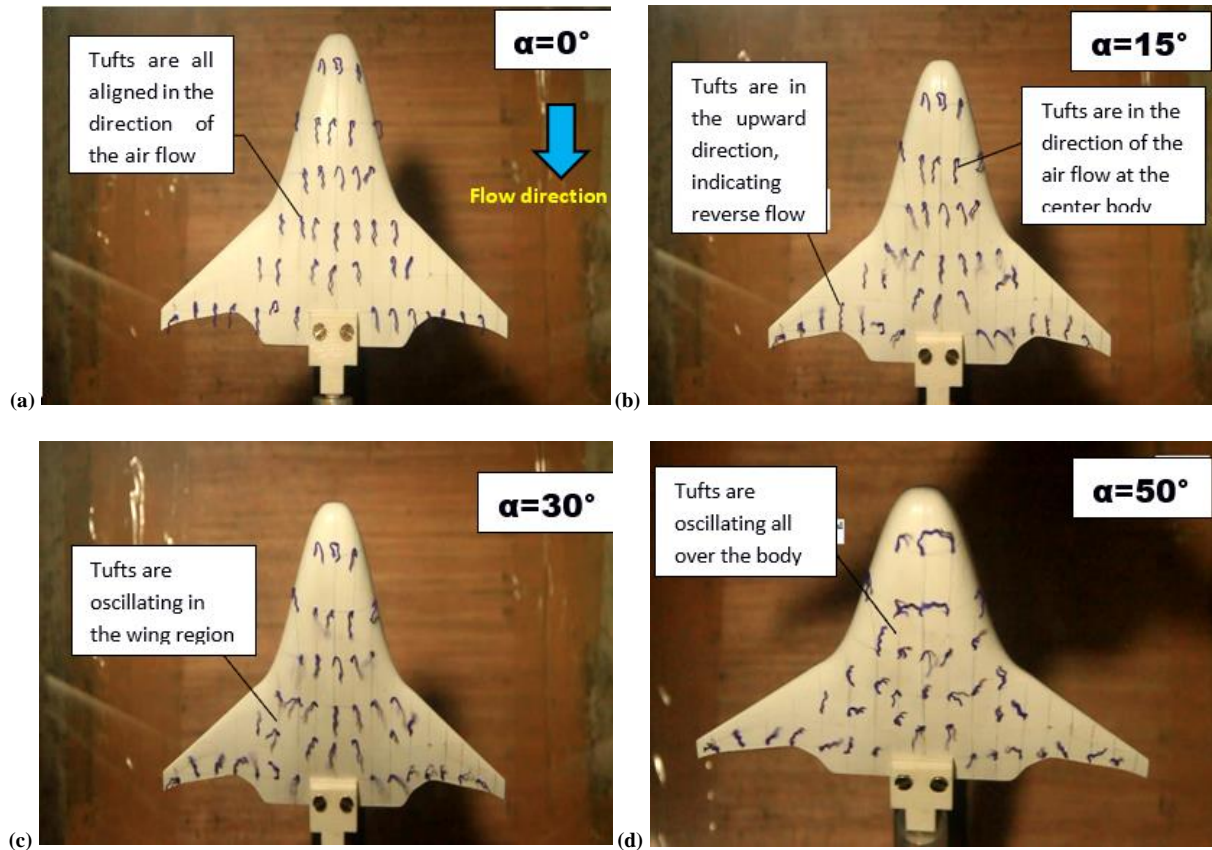


Figure 13: Tuft Flow Visualisation at different angle of attack

4. Conclusion

In the present work, numerical and experimental studies have been performed to understand the complex flow field over a blended wing body at a low subsonic speed. A 3-D BWB model designed in SolidWorks is used for the numerical investigations followed by wind tunnel experiments. A close agreement of the numerical and experimental data is achieved.

The C_L plot obtained from both CFD and experiment shows that the BWB configuration can fly at very high angle of attack (around $\alpha = 45^\circ$) before experiencing stall. The wing has stalled at low angle of attack but the body will still produce lift with increasing angle of attack. Hence, the aircraft body is the main contributor of lift at high angles of attack. Large vortices are observed over the body at an angle of attack around 30° . The spreading of the vortices increases with the increase in angle of attack. For this configuration, the maximum L/D ratio is achieved at $\alpha = 6^\circ$. It is the optimal flight configuration for cruising of this BWB model.

5. Acknowledgement

We wish to thank Mr. Avik Arora, Master's student, Department of Space Engineering and Rocketry, BIT Mesra, Ranchi for his constant support and help during the fabrication process with the 3D printing technology.

6. References

- [1] R. H. Liebeck, “Design of the blended wing body subsonic transport”, *Journal of Aircraft*, Vol. 41, No. 1, pp. 10–25, 2004.
- [2] R. H. Liebeck, M. A. Potsdam, M. A. Page, “Blended wing body Analysis and Design”, AIAA-97-2317, 1997.
- [3] Roberto Merino-Martinez, “Design and Analysis of the Control and Stability of a Blended Wing Body Aircraft”, M. Sc. Thesis, Royal Institute of Technology (KTH), 2015.
- [4] Martin Carlsson and Jakob Kuttenukeuler, “Design and Testing of a Blended Wing Body Aeroelastic Wind-Tunnel Model”, *Journal of Aircraft*, Vol. 40, No. 1, 2002.
- [5] N. Qin, A. Vavalle, A. Le Moigne, M. Laban, K. Hackett, P. Weinerfelt, “Aerodynamic Considerations of Blended Wing Body Aircraft”, *Progress in Aerospace Sciences*, Vol. 40, pp. 321–343, 2004.
- [6] Richard J. Re, “Longitudinal Aerodynamic Characteristics and Wing Pressure Distributions of a Blended Wing Body Configuration at Low and High Reynolds Numbers”, NASA/TM-2005-213754, 2005.
- [7] Sami Ammar, Clément Legros, Jean-Yves Trépanier, “Conceptual design, performance and stability analysis of a 200 passengers Blended Wing Body aircraft”, *Aerospace Science and Technology*, Vol. 71, pp. 325–336, 2017.
- [8] OpenFOAM® - Official home of The Open Source Computational Fluid Dynamics (CFD) Toolbox: <http://www.openfoam.com/> (accessed April 2019).
- [9] NACA 4-digit airfoil generator: <http://airfoiltools.com/airfoil/naca4digit/> (accessed April 2019).
- [10] P. Dehpanah and A. Nejat, “The Aerodynamic Design Evaluation of a Blended-Wing-Body Configuration”, *Aerospace Science and Technology*, Vol. 43, pp. 96–110, 2015.
- [11] D. J. Thompson, J. Feys, M. D. Filewich, Sharif Abdel-Magid, D. Dalli, and F. Goto, “The Design and Construction of a Blended Wing Body UAV”, AIAA 2011-841, 2011.